FULL PAPER

Magnetic Resonance in Medicine 00:00–00 (2016)

Improved Cardiac Magnetic Resonance Thermometry and Dosimetry for Monitoring Lesion Formation During Catheter Ablation

Valéry Ozenne,[1,2]* Solenn Toupin,[1,2,3] Pierre Bour,[1,2] Baudouin Denis de Senneville,[4] Matthieu Lepetit-Coiffé,[3] Manuel Boissenin,[1,2] Jenny Benois-Pineau,[5] Michael S. Hansen,[6] Souheil J. Inati,[7] Assaf Govari,[8] Pierre Jaïs,[1,9] and Bruno Quesson[1,2]

Purpose: A new real-time MR-thermometry pipeline was developed to measure multiple temperature images per heartbeat with $1.6\times1.6\times3\,mm^3$ spatial resolution. The method was evaluated on 10 healthy volunteers and during radiofrequency ablation (RFA) in sheep.

Methods: Multislice, electrocardiogram-triggered, echo-planar imaging was combined with parallel imaging, under free breathing conditions. In-plane respiratory motion was corrected on magnitude images by an optical flow algorithm. Motion-related susceptibility artifacts were compensated on phase images by an algorithm based on Principal Component Analysis. Correction of phase drift and temporal filter were included in the pipeline implemented in the Gadgetron framework. Contact electrograms were recorded simultaneously with MR thermometry by an MR-compatible ablation catheter.

Results: The temporal standard deviation of temperature in the left ventricle remained below 2 °C on each volunteer. In sheep, focal heated regions near the catheter tip were observed on temperature images (maximal temperature increase of 38 °C) during RFA, with contact electrograms of acceptable quality. Thermal lesion dimensions at gross pathology were in agreement with those observed on thermal dose images.

Conclusion: This fully automated MR thermometry pipeline (five images/heartbeat) provides direct assessment of lesion formation in the heart during catheter-based RFA, which may improve treatment of cardiac arrhythmia by ablation. **Magn Reson Med 000:000–000, 2016. © 2016 Wiley Periodicals, Inc.**

Key words: arrhythmia; cardiac; electrophysiology; MR thermometry; radiofrequency ablation

INTRODUCTION

Catheter ablation using radiofrequency (RF) energy is used commonly to treat cardiac arrhythmia when antiarrhythmic drugs fail, with approximately 200000 procedures in Europe in 2012 (1). During this procedure, RF energy is applied to the electrode in contact with the cardiac tissue, inducing a strong current density and an increase in tissue temperature (resistive heating) that may permanently kill the cells when it reaches 60 °C (2). Currently, there is no direct assessment of lesion formation during RF delivery. Some predictions of lesion size and depth have been made based on contact force in bench and in vivo animal studies. However, they are still far from perfect. From both a safety and efficacy stand point, the ideal lesion is transmural, with no extracardiac extension and damage, but with complete cell destruction to prevent cell recovery and arrhythmia recurrence. These features are necessary to reduce the likelihood of severe complications such as atrioesophagial fistulas or tamponade (resulting from a "pop") and to prevent pulmonary vein reconnections that occur in up to 30% of atrial fibrillation (AF) ablation procedures. These examples taken from AF ablation are also valid for other types of complex arrhythmia such as ventricular tachycardia (VT) or atrial tachycardias (ATs), in which both safety and efficacy are limited by the absence of direct lesion formation monitoring.

Direct monitoring of tissue temperature during RF delivery could dramatically improve both the safety and efficacy of cardiac ablation. MRI thermometry, frequently based on proton resonance frequency shift (PRFS) imaging (3), has been developed over the last decade and clinically applied to a wide range of organs (eg, uterus, brain, liver, kidney) for online monitoring of the thermal treatment of various diseases (eg, uterine fibroid, bone metastasis, liver cancer, essential tremor) with demonstrated benefits (4,5). Cardiac thermometry is by far the most challenging because of the combined respiratory and cardiac motion that may induce changes in proton phase and therefore errors in temperature measurements.

[1]Institut Hospitalo-Universitaire, Liryc Institut de Rythmologie et Modélisation Cardiaque, Fondation Bordeaux Université, Bordeaux, France.

[2]Inserm U1045 Centre de Recherche Cardio-Thoracique de Bordeaux, Université de Bordeaux, Bordeaux, France.

[3]Siemens Healthcare France, Saint Denis, France.

[4]Mathematical Institute of Bordeaux, Bordeaux, France.

[5]LaBRI, CNRS, Université of Bordeaux.

[6]Magnetic Resonance Technology Program, National Heart, Lung and Blood Institute, National Institutes of Health, Bethesda, MD.

[7]National Institute of Mental Health, National Institutes of Health, Bethesda, MD.

[8]Biosense Webster, Diamond Bar, CA.

[9]Centre Hospitalier Universitaire de Bordeaux, Bordeaux, France.

*Correspondence to: Valéry Ozenne, Ph.D., Institut Hospitalo-Universitaire, Liryc Institut de Rythmologie et Modélisation Cardiaque, PTIB, Hôpital Xavier Arnozan, Avenue Haut Lévêque, 33604 Pessac, France. Telephone: + 33 5 35 38 19 52; E-mail: Valery.Ozenne@ihu-liryc.fr

Received 11 September 2015; revised 14 January 2016; accepted 18 January 2016

DOI 10.1002/mrm.26158

Published online 00 Month 2016 in Wiley Online Library (wileyonlinelibrary.com).

Furthermore, the blood flow in the cardiac cavities can affect the image quality, thereby reducing the accuracy of temperature mapping. To overcome these problems, several strategies have been proposed, such as hybrid referenceless and multibaseline subtraction (6), or navigator echoes combined with blood suppression techniques (7). Hey et al (7) compared several strategies to cancel the blood signal in the cavities to improve image-based registration techniques. Although performed at 3 T, the gain in signal-to-noise ratio (SNR) could not be used to improve the spatial resolution of the thermometry sequence. To be clinically relevant, cardiac MR thermometry should provide imaging at least every second, with at least 2-mm spatial resolution to allow real-time monitoring of tissue temperature and therefore lesion formation. In addition, dedicated MR-compatible instrumentation must be used to allow RF ablation (RFA) and contact electrophysiology signal recording. A number of studies have reported the use of fully MRI-guided clinical electrophysiology (EP), demonstrating that safety issues (eg, risks of catheter heating by MRI pulse sequence) can be solved (8). Three-dimensional (3D) catheter tracking has also been demonstrated using either passive (9,10) or active methods (11,12), and RFA inside an MRI bore was also successfully reported recently (13,14). Only a limited number of studies (15–17) have reported attempts to address the challenges of cardiac MR thermometry to monitor ablation in real time. Volland et al (15) investigated the feasibility of acquiring limited fields using local MR coils to increase signal sensitivity. In de Senneville et al (17), a single-shot echo planar imaging (EPI) was synchronized with the surface electrocardiogram (ECG) to allow acquisition of several slices per heartbeat. In addition, slice position was continuously updated from echo-navigator readings acquired at the liver-lung interface to reduce respiratory motion and residual in-plane motion, and susceptibility artifacts were compensated with an atlas-based correction technique. However, visualization of temperature increase was restricted to a limited number of pixels in an in vivo sheep heart during RFA, as a result of insufficient spatial resolution ($2.5\times2.5\times6\,mm^3$) and the nonirrigated catheter. Moreover, temperature uncertainty remained too large to evaluate the thermal lesion.

The present study proposes an improved cardiac MR-thermometry method operating at 1.5 T and displaying several slices per heartbeat with increased spatial resolution ($1.6\times1.6\times3\,mm^3$) to resolve temperature distribution in the myocardium during RFA. To this end, a fully automated cardiac thermometry pipeline was developed to allow online monitoring of cardiac temperature. The method relies on ECG-triggered EPI acquired under free breathing, associated with parallel imaging and in-plane motion correction using an optical flow algorithm, allowing voxelwise registration of all incoming temperature maps on the fly. A principal component analysis (PCA) method was implemented to compensate for any motion-related susceptibility artifacts on phase images that do not require an explicit measurement of all heart positions during the preparation phase. Moreover, real-time correction of phase drift is also proposed and a temporal filter was implemented to increase temperature precision with minimal impact on measurement latency. The method was first evaluated in 10 healthy volunteers under free breathing. This fully automated pipeline compensates for the different sources of artifacts and overcomes the current limitations of cardiac MR thermometry. Online determination of the cumulative thermal dose was finally evaluated on a large animal model during RF ablation performed with an irrigated, MR-compatible RFA catheter, allowing simultaneous recording of contact electrograms and lesion assessment through online MR-thermal dosimetry.

METHODS

Volunteer Study

Ten healthy volunteers (31 ± 6 years) were scanned to assess temperature stability under free breathing conditions. Each volunteer was informed about the protocol and consented to participate in the study.

Animal Study

The animal experiment was approved by the ethics committee of the University of Bordeaux. One adult sheep (50 kg) was sedated by intramuscular injection of 1 mg/kg acepromazine (Calmivet, Vetoquinol, Lure, France) and anesthetized by an intravenous injection of ketamine (40mg/kg/h, IM, Virbac, Carros, France) and 2 mg/kg/h midazolam (Mylan, Canonsburg, Pennsylvania). General anesthesia was maintained using continuous intravenous injection of 40 mg/kg/h ketamine and 2 mg/kg/h midazolam. After induction of anesthesia, the animal was intubated, ventilated, and then installed in a supine position on an MR/X-ray-compatible stretcher (Ferno, SMSp, France). The right femoral vein and artery were cannulated with an 8 French sheath. Two MRI-compatible RFA catheters (Biosense Webster, Diamond Bar, California) were advanced and positioned into the right ventricle (for cardiac pacing) and the left ventricle (for ablation) under fluoroscopic guidance (Toshiba InfiniX, Toshiba Medical, Nasu, Japan). Each catheter was 2.66 mm in diameter (8 French) with four electrodes located near the tip (a large one at the tip for ablation followed by three smaller rings, all being used for contact EP recordings), identical to standard, non-MRI-compatible ablation catheters. Right ventricle pacing was chosen to reduce the likelihood of commonly observed ventricular arrhythmia induced by catheter ablation in large animal models. After positioning the catheters, the animal was moved to the MR lab for temperature imaging using the stretcher to avoid catheter displacement. Once the MR-guided RFA experiment was completed, the animal received a lethal intravenous dose of Dolethal (Vetoquinol, Lure, France), and the heart was excised for gross pathology analysis. The heart sample was dissected in thin (~5 mm) slices from base to apex. Each slice surrounding the different positions of the catheter was photographed. In cases in which a lesion could be identified at visual inspection, its dimensions were measured with a ruler.

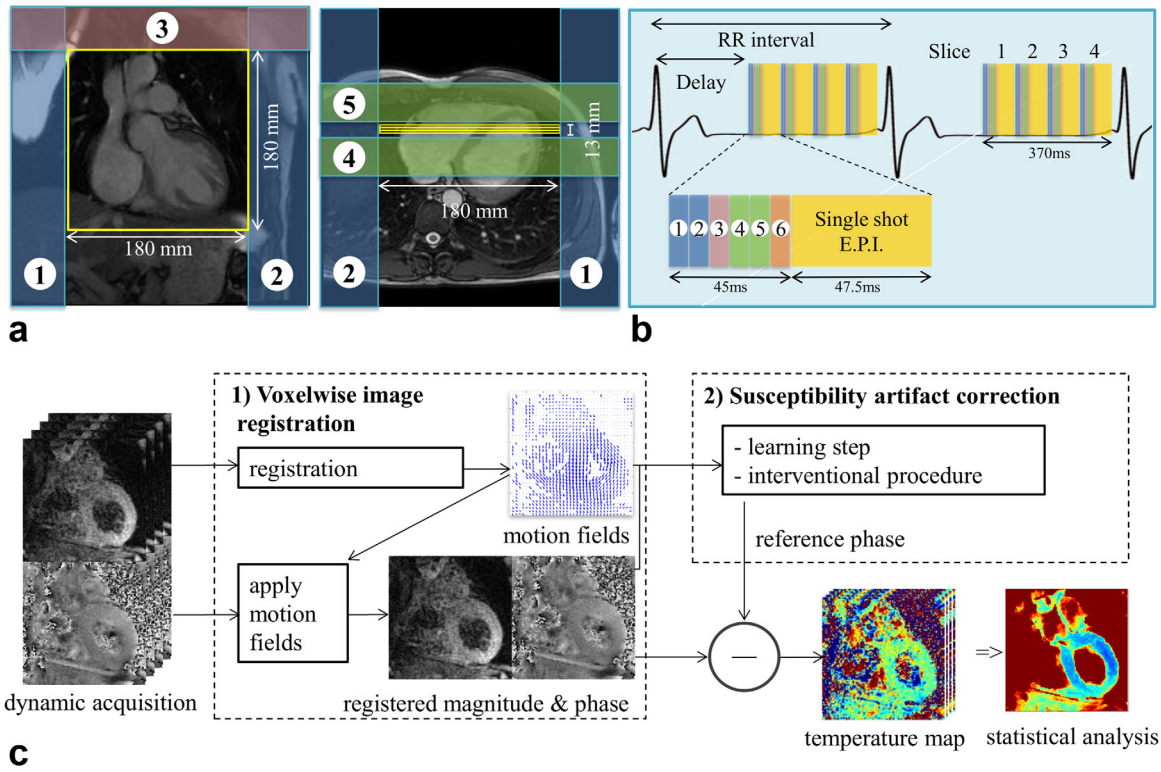

FIG. 1. Real-time cardiac magnetic resonance thermometry pipeline. (**a**) bSSFP images in coronal and transversal orientation on a volunteer showing slice and sat band positioning for cardiac thermometry in coronal orientation. Two saturation slabs are positioned along the FOV (labeled 1 and 2) in the phase-encoding direction. Additional saturation bands (3, 4, and 5) are set parallel and perpendicular to the imaging slice to reduce the signal from blood. The gap between the sat slabs 4 and 5 and slice stack is 5 mm. (**b**) Timing of MR thermometry acquisition relative to the RR interval. Labels 1, 2, 3, 4, and 5 on the insert are the saturation slabs and label 6 represents the fat saturation. (**c**) Dynamic MR imaging is performed using ECG triggering under free breathing. Intrascan motions are compensated for using a nonrigid registration algorithm: Estimation of displacements on a pixel-by-pixel basis results from the analysis of intensity conservation between incoming magnitude image and a reference image. Motion fields are then applied to phase images to follow specific voxel temperature elevation. To address respiratory-induced susceptibility changes, the LUT method or synthetic modeling phase PCA is initialized during a pretreatment period. These reference data are then subtracted from the incoming registered phase during the interventional procedure.

Radiofrequency Ablation Device and Magnetic Resonance–Compatible Electrophysiology

The tip electrode of the catheter inserted into the left ventricle was connected to a clinical RFA generator (Stockert Medical Solution, Freiburg, Germany) located outside the Faraday cage. During ablation, the catheter was irrigated with continuous flow (17 ml/min) using a saline solution (0.9% concentration) to reduce temperature increase at the catheter–tissue interface and maintain electrical conductivity. The heart was paced to overdrive sinus rhythm using the second catheter with a pulse generator (Agilent, Santa Clara, California). Cables from each catheter were extended and connected to a clinical EP acquisition system Bard (LabSystem PRO, Boston Scientific, Marlborough, Massachusetts) located outside the Faraday cage. Band Reject Filters (attenuation > 40 dB) tuned to the MR proton resonant frequency (64 MHz) were designed and inserted into the transmission line of each electrode. The voltage between the two distal electrodes (1–4) was displayed continuously on the EP console. Each signal was processed on the EP console using a band rejection filter (bandwidth: 1–250 Hz) and a Butterworth low-pass filter (cutoff frequency: 50 Hz).

Magnetic Resonance Data Acquisition

Imaging was performed on a 1.5T MAGNETOM Avanto MR scanner (Siemens Healthcare, Erlangen, Germany) equipped with two 16-channel cardiac coils. Coils were positioned below and above the thorax on the volunteers, whereas on the animal they were positioned lateral to the thorax to maximize the number of elements near the heart. A dynamic, multislice acquisition was performed using a single-shot gradient EPI sequence. Four to five slices in sagittal or coronal orientation (Fig. 1a) were acquired sequentially in ascending order within the same heartbeat, over 250 successive cardiac cycles. The following imaging protocol was used: $180\times180\,mm^2$ field of view (FOV), 110×110 matrix (resulting in an in-plane resolution of $1.6\times1.6\,mm^2$), 3 mm slice thickness, 0.3-mm gap between slices, flip angle = 60°, bandwidth = 1568 Hz/pixel, TE = 19 ms, TR = 92.5 ms, GRAPPA acceleration factor of 2 with 75% partial Fourier acquisition. Two saturation slabs were positioned along the FOV (Fig. 1a) in the phase-encoding direction to avoid aliasing, and three additional saturation bands were set parallel and perpendicular to the imaging slice to reduce blood signal, as suggested in (7). A fat-selective pulse (Gaussian, 5 ms in duration) surrounded by spoiler gradients was used

to cancel the lipid signal. All saturation slabs were played before each slice (Fig. 1b). The effective slice update time was given by the cardiac cycle duration, as the sequence was ECG-triggered. The delay between QRS detection and the beginning of the acquisition of the first slice was adjusted manually to ensure that all slices could be included within a single heartbeat. Depending on the cardiac cycle duration and number of slices, this corresponded to mid/end diastolic phases.

Thermometry Pipeline

Raw data were streamed through TCP/IP to the Gadgetron framework for online image reconstruction (18). The pipeline was run on a Core i7-4790 processor (3.6 GHz, four cores, INTEL Santa Clara, California) operating under Linux and including EPI ghost-correction and GRAPPA (19) reconstruction. Several additional modules ("gadgets") were implemented in house and inserted into this framework for real-time thermometry. This included motion correction using Graphics Processing Unit (GPU) graphic cards (Quadro K620, NVIDIA, Santa Clara, California) and susceptibility artifact correction (see subsequently for implementation details). The resulting temperature images were sent to a remote host computer for display on dedicated thermometry software (Thermoguide, IGT, Pessac, France). All data were transferred by TCP/IP networking on a subsecond timescale.

Image Registration

Through-plane motion was minimized by setting the imaging plane in sagittal or coronal orientation to visualize the heart displacement related to respiratory motion. An optical flow algorithm (20) was used to register in-plane motion on magnitude and phase images at a fixed position and to compute displacement field *(U,V)* for each acquisition as previously published (7,21). To deal with large displacement amplitudes (~2 cm for respiration, corresponding to 12 pixels), a coarse-to-fine multiresolution approach was used, which iterated the optical flow algorithm on an image pyramid with four levels up to the original image resolution (22,23). The reference image was automatically picked at the center of the respiratory cycle using the following method: 1) The first 10 magnitude images were registered on the first image independently for each slice; and 2) the resulting motion fields were averaged and sorted to find the median position in the respiratory cycle in the largest displacement axis. Once this automatic reference image was selected, the temperature calculation was performed iteratively on each new incoming data set.

Correction of Respiratory-Induced Susceptibility Changes and Temperature Calculation

Respiratory-related susceptibility effects were corrected using two alternative multibaseline correction strategies (a "look-up table" (LUT) based method (24) and a PCA-based method (25)) to compare the temperature accuracy in the context of cardiac thermometry. Although the LUT-based method was solely restrained to positions observed during the learning step, the PCA-based method extended the correction to nonobserved positions. For both methods, a learning step (30 dynamic acquisitions, lasting approximately 30 s) was performed to generate reference data that were used during the interventional procedure (210 dynamic acquisitions, approximately 3′30 min) (Fig. 1c). The PCA-based method collected optical flow fields from registration during the learning step and built a parameterized flow model using the PCA algorithm. The overall magnetic field variations were approximated as the sum of linear phase changes of each motion descriptor (noted as D_j) on a pixel-by-pixel basis, giving a parameterized magnetic field model (noted as B_j) (25). During the intervention, the largest PCA-based motion descriptors were estimated from the current flow field of magnitude images and used to reconstruct the background phase (φ_{REF}) distribution from the parameterized model (details on the PCA component determination (N) can be found in (25)):

$$\varphi_{\mathrm{REF}}(\mathrm{x},\mathrm{y}) = \sum_{\mathrm{j}=0}^{\mathrm{N}-1} \mathrm{D_j}.\mathrm{B_j}(\mathrm{x},\mathrm{y}) + \mathrm{B_N}(x,y) \qquad [1]$$

where N represents the dimension of the PCA-based decomposition (ie, number of Eigen vectors and associated Eigen values); B_j are the Eigen vectors maps resulting from the PCA on the data acquired during the learning step; and B_N is the phase value in each pixel that does not vary with respiration. The three Eigen vectors with the highest Eigen values were selected to compute the synthetic reference phase map. The sum of these three Eigen values represented more than 95% of the Eigen values resulting from the PCA. The synthetic phase φ_{REF} was subtracted from the experimental phase and the temperature was computed using the PRFS ($\alpha = -0.0094$ ppm/°C) (3).

Spatio-Temporal Phase-Drift Correction

Potential phase drift over the 4 min of acquisition was approximated as a spatio-temporal first-order polynomial function:

$$P(x,y,t) = a.x + b.y + c.t + d \qquad [2]$$

where, *a, b, c*, and *d* are parameters to be defined from experimental temperature images. For each slice, each new magnitude image registered to the reference position was averaged with all previously acquired images. Regions with low SNR on the resulting averaged magnitude images were masked out using a threshold value equal to three times the standard deviation of the noise. A second mask was computed to remove all voxels with a temporal standard deviation of temperature (TSD) higher than a predefined threshold (a typical value of 4 °C was employed in this study). For this purpose, the TSD and temporal mean (μ_T) images were computed iteratively for each slice using the following formulas:

$$\mu_{d+1} = \frac{\mathscr{T}_{d+1}}{d+1} + \frac{d}{d+1} * \mu_d \quad \text{and}$$
$$TSD_{d+1} \approx \frac{(\mathscr{T}_{d+1} - \mu_{d+1})^2 + d \cdot TSD_d}{d+1} \qquad [3]$$

where *d* is the dynamic number and T_d the temperature map at dynamic number d.

On the last available temperature image, regions with temperatures over 5 °C were masked out to automatically exclude the heated regions close to the catheter. A resulting mask was computed using the intersection of the three masks (magnitude, TSD, and temperature). The fit to Eq. [2] was performed on the last 20 temperature images using pixels included in this mask. A temporal sliding window of 20 dynamic acquisitions starting at the beginning of the interventional procedure (no correction was applied for the first 20 dynamic acquisitions) was used to iteratively update the coefficients (*a, b, c, d*) for each slice, using a root-mean-square error minimization algorithm. Once the coefficients were calculated, a temperature drift map was subtracted to the incoming temperature map and updated by moving the sliding window to the next dynamic acquisition.

Temporal Temperature Filtering

An optional additional temporal temperature filtering was implemented to convert temporal resolution into temperature precision, taking advantage of the registration of all temperature images at a common reference position. For this purpose, a first-order low-pass Butterworth filter with a cutoff frequency of 0.14 Hz was inserted at the end of the pipeline. No spatial filtering was included in the pipeline.

Thermal Dose Calculation

The cumulative thermal dose (TD) was computed from the temperature images using the Sapareto equation (26), taking an equivalent dose of 240 min at 43 °C as a lethal threshold. As uncertainty on temperature estimates influences the thermal dose calculation (27,28), the lethal thermal dose threshold was corrected on each pixel to account for TSD maps, using the following formula:

$$TD_{corr}(x,y) = TD(x,y) * e^{-0.5\times\left(\ln(2)\times TSD(x,y)\right)^2} \quad [4]$$

TSD was estimated on each pixel surrounding the catheter before RF delivery (over 20 dynamic acquisitions).

Statistical Analysis

To assess the quality of the temperature measurements without heating, the TSD and μ_T were calculated for each pixel. For this evaluation, during the interventional procedure all 210 dynamic acquisitions of the four slices for the 10 volunteers and two orientation planes (in total 16800 images) were used. For each slice, motion-registered magnitude images were averaged over all dynamic acquisitions. Then, a region of interest (ROI) surrounding the ventricle was manually drawn on each resulting slice. The μ_T and TSD distributions integrating all slices were plotted with a box and whisker graphical representation using five different distribution percentages: T10, T25, T50, T75, and T90, corresponding to 10, 25, 50, 75, and 90% of the distribution of the TSD values, respectively. The same analysis was repeated after temporal filtering.

RESULTS

Volunteer Temperature Imaging

The mean ± standard deviation (SD) heart rate across all volunteers was 67 ± 10 bpm, with minimal and maximal values of 44 and 83 bpm, respectively. Figure 2 shows an example of thermometry results obtained on a volunteer at 1.6x1.6x3 mm^3 resolution using the PCA-based method to compensate for respiratory-related susceptibility artifacts. Figures 2a and 2b display the averaged (over 240 dynamic acquisitions) registered magnitude images in coronal and sagittal views, respectively. In each slice, the image showed a well-delimited frontier between the myocardium and adjacent organs (liver, lungs). The proximal aorta, left atrium, and aortic valve could be identified, which is indicative of a successful image registration. Residual blood signal could be observed on each slice, with increased suppression for the last images acquired at the end of diastole.

Figures 2c and 2d display the TSD maps for the corresponding slices, overlaid on an averaged registered magnitude image (Fig. 2a and 2b). In the coronal view, most of the pixels displayed a TSD at approximately 2 °C over the myocardium, including a large part of the left ventricle (LV) and only the inferior part of the right ventricle (RV). In the sagittal view, temperatures in both the LV and RV could be mapped.

In the coronal view, the TSD (mean ± SD) in each slice was 2.42 ± 0.93 °C, 2.26 ± 1.05 °C, 2.11 ± 1.22 °C, and 2.23 ± 1.09 °C (2.25 ± 1.10 °C over all slices). In the sagittal view, the TSD was 2.10 ± 0.75 °C, 2.08 ± 0.75 °C, 1.86 ± 0.90 °C, and 1.90 ± 0.90 °C (1.98 ± 0.80 °C over all slices), respectively. The sizes of the ROIs were 1265 ± 245 pixels and 952 ± 168 pixels, respectively. The temporal mean of temperature for the corresponding data sets were –0.07 ± 2.50 °C and –0.05 ± 0.40 °C, respectively. Additional temporal filtering with the Butterworth low-pass filter resulted in a TSD of 1.12 ± 1.3 °C in coronal view and 0.82 ± 0.40 °C in sagittal view (Fig. 2e and 2f), with a temporal mean of temperature of –0.10 ± 2.30 °C and 0.01 ± 0.4 °C, respectively. Figure 2g displays the temporal evolution of the temperature in a single voxel at each step of the image processing pipeline. Large amplitude oscillations (approximately higher than ± 10 °C) remain visible after motion correction (orange curve), as a result of respiratory-related susceptibility effects. After PCA correction, these oscillations are reduced, showing the temporal phase drift (yellow curve) that is corrected by the processing method (blue curve). TSD is improved by additional low-pass Butterworth temporal filtering (green curve). The mean ± TSD values in the pixel at each step were –2.7 ± 5.7 °C, –1.4 ± 0.9 °C, –0.1 ± 0.9 °C, and –0.1 ± 0.4 °C, respectively.

The statistical analysis of temperature distribution over all volunteers is presented in Figure 3 using box and whisker plots, for the three motion-related susceptibility-correction methods (LUT, PCA, and PCA with temporal filtering). Nonuniform phases were observed at the heart-liver-lung interface in all volunteers. This small region (less than 4% of the ROI) containing unwanted artifacts was removed from the analysis. Across all correction methods, the temperature offset (Fig. 3b)

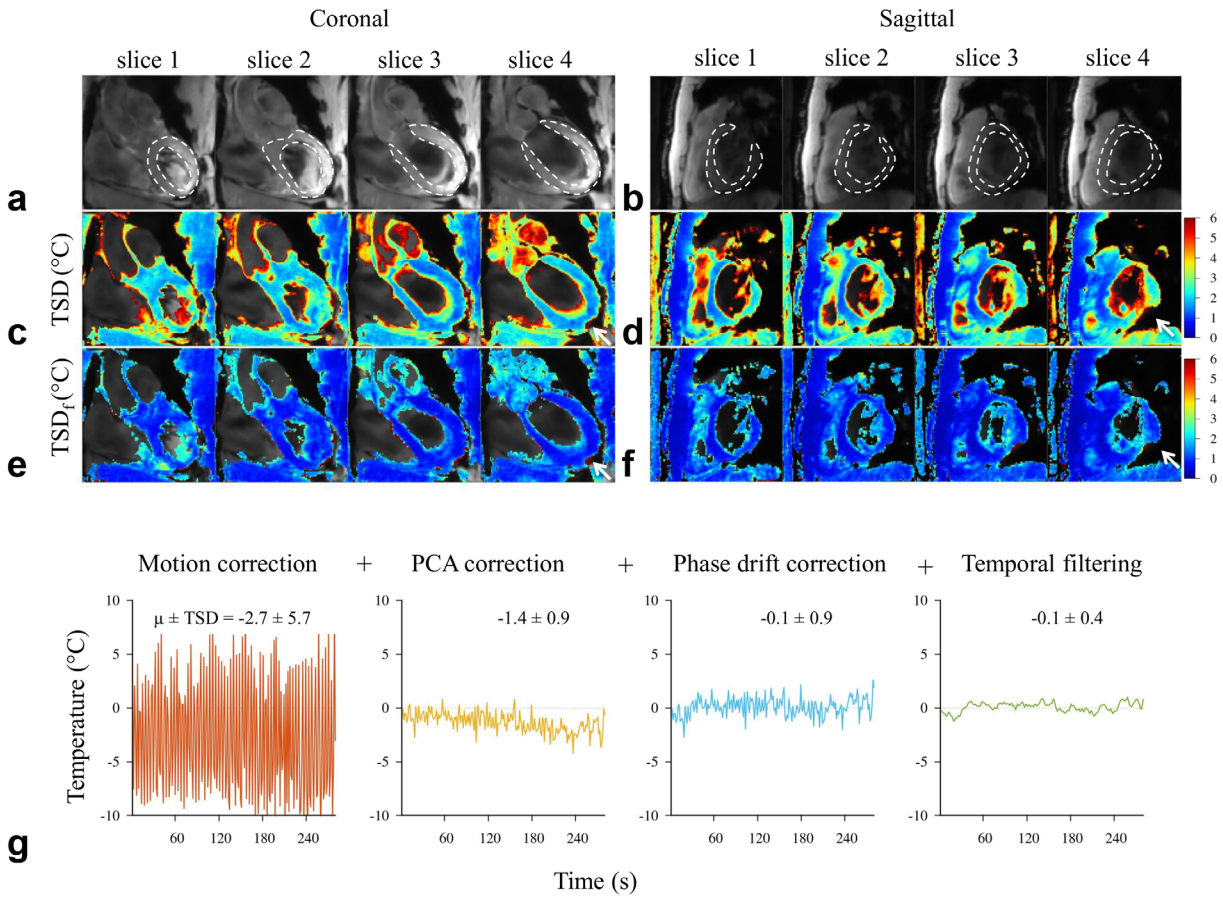

FIG. 2. Thermometry evaluation on a human volunteer measured at 1.6×1.6×3 mm^3 resolution using the PCA-based method, in coronal and sagittal views. Temporal standard deviation temperature maps (c and d) are overlaid on averaged registered magnitude images (a and b). A total of 210 dynamic acquisitions were used for calculating TSD temperature and for averaging the registered magnitude images. Dotted lines in (**a**) and (**b**) show contour of the myocardium used for the statistical analysis of temperature data. Presence of large phase variations or low SNRs resulted in increased TSD only in small areas (white arrow). Images (**c**) and (**d**) are TSD using the PCA-based method and temporal filtering (low-pass Butterworth filter with 0.14-Hz cutoff frequency). (**e**) Temperature evolution versus time in a single voxel (taken from the sagittal view, slice No. 2) at different steps of the pipeline: after motion correction (orange curve), after PCA correction of susceptibility artifacts (yellow curve), after phase drift correction (blue), and after temporal filtering (green curve). At each step, the temporal mean and TSD values within this voxel are also indicated.

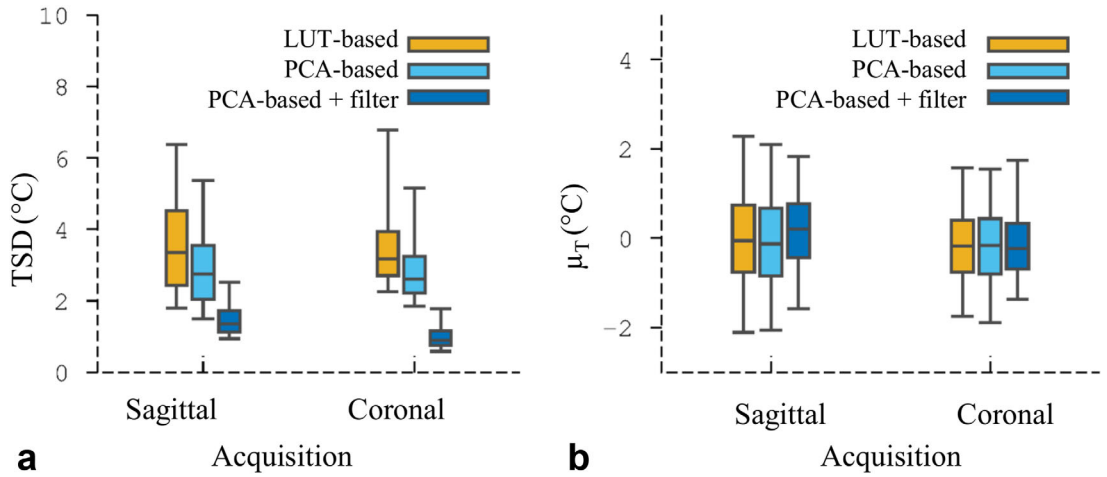

FIG. 3. Statistics on 10 healthy volunteers during free-breathing acquisition. Box-and-whisker plots of the distribution of temperature TSD (**a**) and offset (**b**) over all volunteers, with the LUT method, PCA, and PCA+filtering methods. The data were retrieved from ROIs (see Fig. 2a and 2b) surrounding the left ventricle using all dynamic images for each orientation plane.

remained close to zero for both image orientations. The TSD was systematically higher with the LUT-based method as compared with the PCA-based method (Fig. 3a). In the sagittal view, the T50/T75 values were 3.35/4.52 °C and 2.74/3.55 °C, respectively. In the coronal view, the T50/T75 values were 3.17/3.93 °C and 2.60/3.25 °C, respectively. The TSD distributions resulting from the LUT and PCA methods were statistically different (Student's t-test, $P < 0.001$). Temporal filtering had a negligible effect on the temperature offset, but reduced the temporal standard deviation of temperature by a factor of two or more, with T50/T75 values of 1.36/1.72 °C in the sagittal view and 0.90/1.15 °C in the coronal view.

In Vivo Radiofrequency Ablation of the Left Ventricle in a Sheep

During the intervention, the heart was paced at 86 bpm (700 ms cycle length) to reduce the risk for ventricular arrhythmia during RFA. Four RFA of 60 s each were performed successively at different locations in the left ventricle with a progressive increase of RF power from 15 to 30 W in each.

Figure 4a shows one example of thermometry data during RFA, with the catheter visible in slice No. 2 on the time-averaged registered magnitude images. Phase distribution in pixels surrounding the catheter tip did not show phase wraps that could alter temperature precision (Fig. 4b). μ_T and TSD maps were computed before the interventional procedure over 20 consecutive dynamic acquisitions for the five slices acquired in a sagittal orientation on the myocardium (zoomed view in Fig. 4c), using the PCA method for susceptibility compensation and temporal filtering. The resulting values (mean ± SD) were $\mu_T = -0.13 \pm 0.41$ °C and TSD = 0.67 ± 0.24 °C, respectively. The sizes of the ROIs shown in Figure 4a were 517 ± 152 pixels. Figure 4d displays the five temperature images after 42 s of heating at 26 W. A local temperature increase can be observed in the myocardium at the contact of the catheter tip with a less intense temperature increase at the same level in adjacent slices. In Figure 4e, temporal evolution of temperature in slice No. 2 are plotted on a 6x6 mm^2 voxel area centered on the heated region (red curves), together with temperature values away from the catheter area (black curves). On each pixel, a progressive heating with a maximal temperature increase of 28 °C at the contact with the catheter can be observed. After switching off the RF energy, the temperature decreased in all pixels. However, the temperature decrease was faster in the three pixels at the point of catheter contact, with a final temperature lower than the preablation temperature in two of them. This was attributed to the catheter tip cooling with saline solution infusion at room temperature. In pixels located away from the contact zone, the temperature decrease was slower and returned to its initial value.

Table 1 reports the thermometry results for the four RF procedures performed on the sheep. The maximal temperature rise in the three slices surrounding the catheter tip increased with the applied RFA power from 13 °C (15 W) to 38.9 °C (30 W). The cumulative thermal dose was computed for each experiment. The temperature increase was insufficient in the experiments performed at 15 and 17 W to reach the lethal threshold. At 26 W, only 6 pixels in the central slice reached the lethal value, but at 30 W the lethal thermal dose was reached in 21 pixels in the central slice and in 7 and 10 pixels in the adjacent slices, respectively.

Figure 5 shows the electrograms recorded with the ablation catheter, before, during and after RFA, for the experiment reported in Figure 4. Slight changes in signal could be observed as the ablation advanced; however, there were limited artifacts during RF delivery and/or MR sequence acquisition, demonstrating excellent feasibility.

Figure 6 displays the thermal dose images (a and b) and gross pathology (c and d) for the experiments performed at 26 W (left column) and 30 W (right column) on the sheep. Neither focal ablation nor hemorrhage could be visualized from the endocardial surface for the two RF deliveries performed at 15 and 17 W (data not shown). The experiment performed at 26 W resulted in 6 pixels reaching the thermal dose (Fig. 6a) and showed traces of hemorrhage (Fig. 6c) at the surface of the endocardium. The experiment performed at 30 W resulted in 21 pixels reaching the lethal thermal dose threshold (Fig. 6b) and showed a focal, semicircular, ablated area with a central white zone surrounded by a red hemorrhagic ring (Fig. 6d) at gross pathology. Dimensions of this lesion were approximately 6x8 mm^2, which is in good agreement with the dimensions observed on the thermal dose image.

DISCUSSION

In this study, we demonstrate the possibility of mapping temperature distribution in the myocardium during free breathing in humans with only 1 °C of uncertainty, an update rate given by the cardiac cycle duration (~1-s time scale), an in-plane spatial resolution of 1.6x1.6 mm^2, and a slice thickness of 3 mm. Compared with the published data (15,17) in which the voxel size was 2.5x2.5x6 mm^3 or more, the spatial resolution in the present work improved five-fold and the temperature precision improved to 1 °C uncertainty. Therefore, this precision allows better visualization of the temperature distribution during RFA on an animal model. This thermometry pipeline combines rapid imaging with online reconstruction (including GRAPPA reconstruction and EPI corrections), motion correction, and susceptibility compensation using the two different methods. The quantitative analysis of TSD showed that the LUT-based and PCA-based susceptibility compensations can provide reliable thermometry, although the PCA method was found to be slightly superior. In an animal model, very regular breathing (12 Hz) imposed by mechanical ventilation ensured reliable temperature estimates with lower TSD values (SD = 0.67 ± 0.24 °C). The adjunction of temporal filtering with a conventional low-pass Butterworth filter improved the TSD with a resulting temperature distribution below 2 °C in 75% of the pixels located in the myocardium. Simulations of the latency induced by this filter revealed limited impact (delay of three dynamic acquisitions), making it appropriate for online

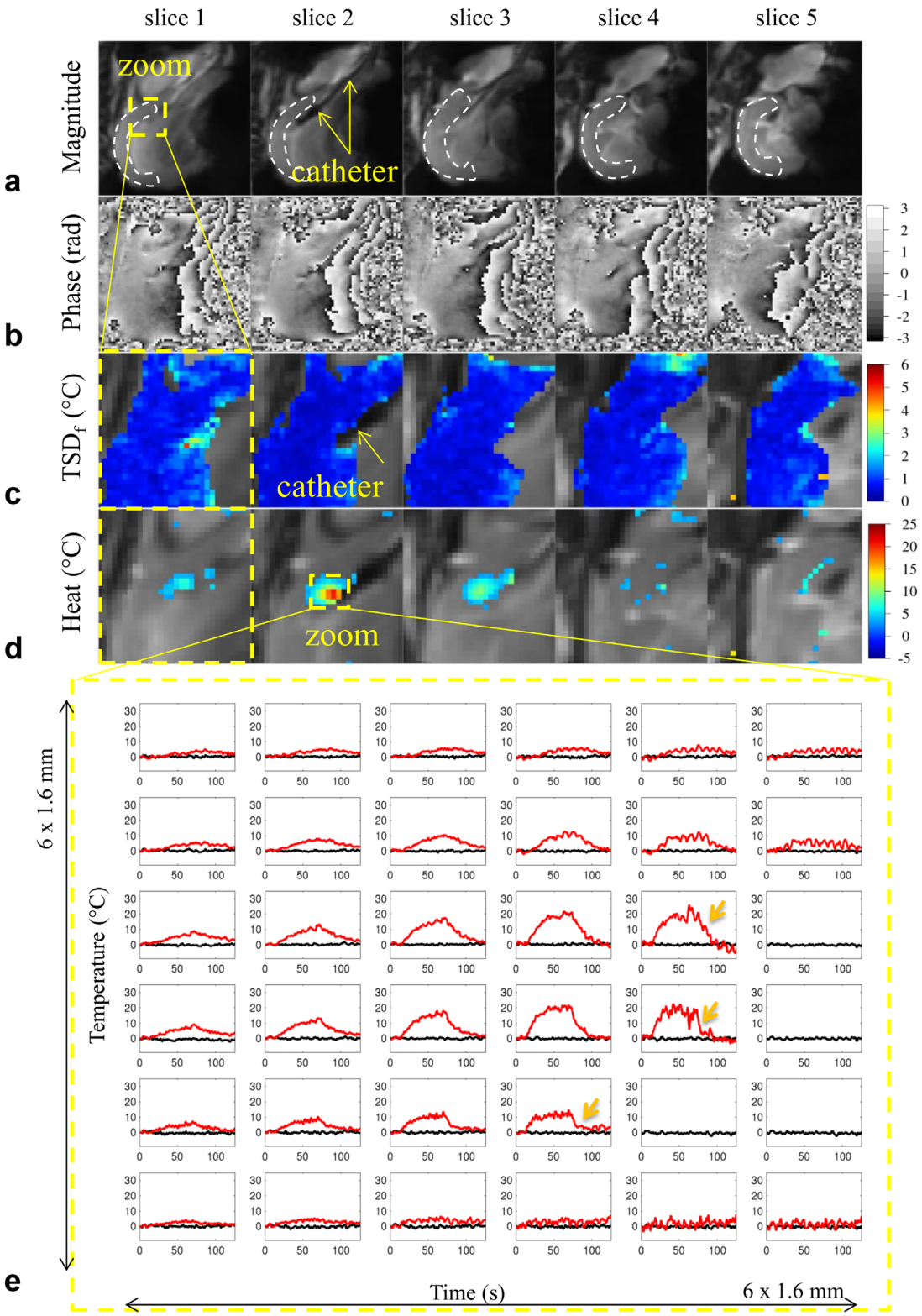

FIG. 4. MR-thermometry monitoring during RFA at 26 W on the left ventricle. Averaged registered magnitude images (**a**). Dotted lines show contour of the myocardium used for statistical analysis of temperature data before RF ablation. Reference phase images (**b**). TSD map (over 20 dynamic acquisitions) in sagittal view overlaid on averaged registered magnitude images before the interventional procedure (**c**). Instantaneous temperature at acquisition No. 120 (**d**). A second zoom view (**e**) shows temperature elevation as a function of time for each voxel surrounding the catheter (in red). Temperature baseline (in black) from a myocardium region away from the catheter is superimposed as a reference. Orange arrows show rapid temperature decrease in the pixel at the vicinity of the catheter tip.

Table 1
Temperature Data for Several RF Ablations Performed in One Sheep[a]

	Maximal temperature increase (°C)			Number of pixels reaching lethal TD		
RF power (W)	Slice (n–1)	Slice (n)	Slice (n+1)	Slice (n–1)	Slice (n)	Slice (n+1)
15	7	13	5	0	0	0
17	9.8	18.7	11.5	0	0	0
26	13.5	27.7	17.4	0	6	0
30	25.8	38.9	27	10	21	7

[a]Each ablation was performed over 60 s at the power indicated in the first column. The maximal temperature increases are reported in the three slices surrounding the catheter (n–1, n, and n+1). The last three columns provide the number of pixels having reached the lethal thermal dose threshold.

temperature monitoring and potential development of automatic feedback algorithms for optimized energy delivery (29,30) to avoid excessive heating of the myocardium. Although this filter theoretically reduced the temporal resolution of the thermometry method to several seconds, its effect on actual temperature estimates during RFA can be considered negligible because of the slow evolution of temperature in the tissue (Fig. 4e). This pipeline was developed into the Gadgetron reconstruction framework (18), which is being used increasingly in the MRI research community. The process incorporating reconstruction, motion correction, susceptibility compensation, phase drift correction, and temporal filtering was implemented in GPU or C++ in dedicated software modules ("gadgets"), resulting in an overall image latency of 75 ms in its current implementation. The pipeline ensures real-time monitoring for at least 10 slices/s.

In this study, imaging planes were positioned in coronal or sagittal orientations to visualize respiratory motion. Image-based algorithms were then applied to register all images at fixed positions and respiratory-related susceptibility changes were also compensated for. In previous studies, respiratory motion during acquisition was compensated by using slice tracking from navigator readings and images that were oriented in short axis. This method could be advantageous for blood signal cancellation, as blood flow should be better attenuated with inflow saturation using saturation slabs parallel to the imaging plane (7). In the present work, blood signal was attenuated with the same technique, playing saturation slabs 45 ms before each slice. However, the signal remained visible inside the cavities (see slice No. 1 and No. 2 in Fig. 2a) primarily for the first slices acquired in the cardiac cycle, due to limited time for saturated blood to enter the slice. Nevertheless, TSD were not altered, and comparable thermometry quality could be reported (see Fig. 2). For the animal experiment, the blood signal in the cavities remained visible in all slices but did not affect the thermometry results. Averaging the motion-registered magnitude images allowed the visualization of small anatomical structures such as cardiac valves, illustrating the robustness of the image-based correction method. Different strategies have been proposed to remove potential temporal phase drift, such as subtraction of a global temperature offset from a ROI (21). In this study, an automatic phase drift correction was implemented using a first-order spatio-temporal polynomial model. This technique was shown to be efficient in all of the experiments. The first-order spatio-temporal model used to fit the drift may be suboptimal in some locations within the heart, leading to a standard deviation of the mean temperature (μ_T) value in the range of $\pm 2\,^{\circ}C$ (for the volunteer data in Fig. 2 in the coronal orientation). More complex fitting models could be applied to improve the thermometry pipeline, but with the current implementation, residual mean temperature values over all volunteers were found to be acceptable (see distribution in Fig. 3b).

The irrigated, MR-compatible ablation catheter did not produce large artifacts even though a single-shot EPI sequence was used. The effect of the saline infusion flowing from the catheter tip electrode did not alter the temperature image quality, and the effect of local cooling at myocardium contact could be observed on temperature maps demonstrating the performance of temperature monitoring. Increasing the spatial resolution allowed characterization of the temperature distribution in each slice, reducing the influence of the partial volume effect.

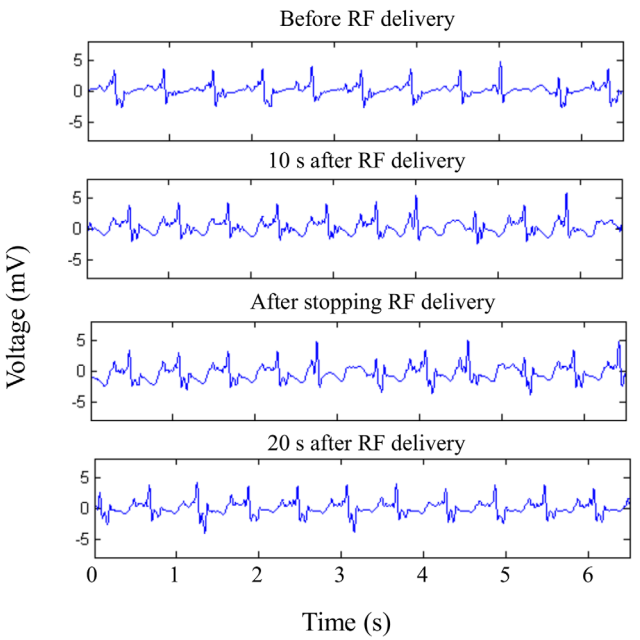

FIG. 5. Contact electrograms acquired during radiofrequency ablation in sheep. Electrograms recorded between the two distal electrodes (1–4) of the MR-compatible catheter for approximately 6 s, before (top trace) RF delivery, after 10 s RF delivery at 26 W (second trace), immediately after stopping RF delivery (third trace), and 20 s after the end of RF delivery (bottom trace).

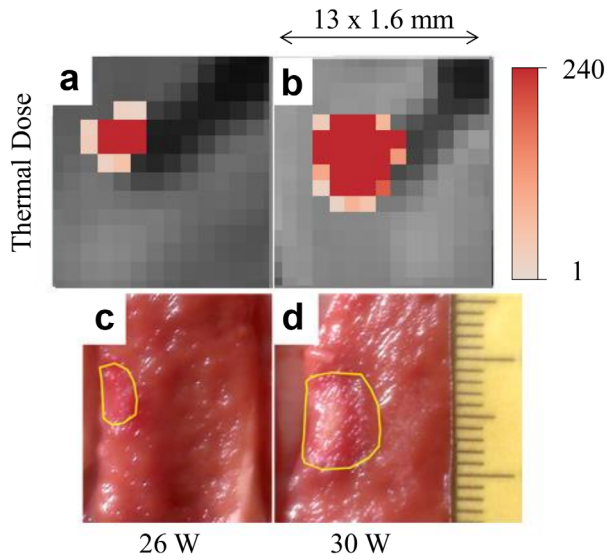

FIG. 6. Cumulative thermal dose images and gross pathology results for the two RFA experiments performed at 26 and 30 W. Pixels having reached the lethal thermal dose threshold superposed on the averaged motion registered magnitude image, for the two ablations performed at 26 W (a) and 30 W (b). Photographs of sections (from endocardium to epicardium) of the LV immediately after sacrifice of the animal, for the corresponding RF power conditions: yellow contours (c and d) delineate the thermal lesion and scale at the right of (d) in millimeters (same zoom factor used in (c) and (d)).

Right-ventricle pacing of the sheep helped to maintain a stable rhythm during ablation. The high incidence of ventricular arrhythmia during RF delivery is specific to large animals such as pigs or sheep and is not an issue in patients. TSD showed superior results to volunteer data and was attributed to a better control of breathing conditions.

Electrograms recording from the ablation catheter could be successfully performed during the whole procedure with a preserved quality, including during MRI acquisition and/or RFA, using analog and numerical filters.

The ultimate objective of this cardiac thermometry pipeline is to provide the physician with a quantitative map of the thermal damage induced by RFA through a direct calculation of the cumulative thermal dose. The two experiments performed at low RF power did not produce thermal damage as reported by the gross pathology analysis. For these experiments, no pixels reached the thermal dose threshold on MR-thermal dosimetry images. In contrast, when the thermal dose threshold was reached on MR-thermal dosimetry, tissue alteration was observed at gross pathology. In the experiment performed at 26 W, only 6 pixels reached the lethal thermal dose and limited superficial damage was observed at gross pathology. In the cases of such moderate heating, the voxel size may be considered too large to assess the thermal dose deposition with sufficient precision to predict the lesion size. For the experiment performed at 30 W, a larger region was heated and a semicircular region of 5 pixels in diameter reached the lethal threshold. With the 1.6-mm in-plane resolution of MR thermometry sequence, this leads to a predicted thermal lesion of 8 mm in diameter, which corresponds well with the gross pathology results (6x8 mm^2 in Fig. 6d).

This online temperature monitoring enables direct lesion mapping and should be compared with strategies such as the calculation of a lesion index (31), which integrate power, time, and contact force values to estimate the RF lesion size.

Study Limitations

Although clinical cardiac MR thermometry appears to be feasible with the proposed method, the present study shows a number of limitations. The thermometry method was evaluated on 10 healthy volunteers and showed accurate temperature estimates on the left ventricle. Although MR thermometry was found to be reliable in more than 90% of the pixels (TSD values below 2 °C in Fig. 3a) included into the ROI surrounding the LV, a few pixels exhibited spatial phase wraps that remained uncompensated with the current processing pipeline (white arrows in Fig. 2). Further image processing methods are under consideration to compensate for this artifact, to retrieve exploitable temperature estimates in these pixels located at the liver-lung-heart interface.

Coronal and sagittal orientations were assumed to fully encompass respiratory motion. However, more refined positioning of the imaging slices may be necessary to increase robustness of the thermometry by reducing potential residual through plane motion, depending on patient anatomy. Future work will investigate the precision of MR thermometry on patients suffering from arrhythmia, allowing quantitative evaluation of motion correction and susceptibility artifact compensation. In this study, a limited number of RFAs were performed in only one animal. Therefore, no statistical correlation between thermal dose and actual lesion size could be performed, although a good correspondence was observed between the thermal dose image and gross pathology analysis for the experiment performed at 30 W. Further studies are needed on a larger number of animals to demonstrate the value of this lesion monitoring strategy. However, this was out of the scope of the present work, which aimed to provide a proof of concept of an improved cardiac MR thermometry method for monitoring tissue temperature during RFA simultaneously with electrogram recording.

CONCLUSIONS

This study proposes a significant step forward toward the clinical applicability of cardiac MR thermometry for online monitoring of temperature changes during RFA. Cardiac MR thermometry will be of benefit if catheter ablation under MR is adopted in clinical practice. It could provide online lesion formation monitoring and would complement postablation lesion imaging by other MR modalities. This approach should allow for significant improvements in safety and efficacy of catheter ablation.

ACKNOWLEDGMENTS

This work received the financial support from the French National Investments for the Future Programs ANR-10-IAHU-04 (IHU Liryc) and Laboratory of Excellence ANR-10-LABX-57 (TRAIL), and the research programs ANR-11-Tec-San-003-01 (TACIT), Equipex ANR-11-EQPX-0030 (MUSIC) and ANR-13-PRTS-0014-01 (MIGAT). We gratefully thank Pippa McKelvie-Sebileau for the manuscript editing.

DISCLOSURE

A. Govari is an employee of Biosense Webster. The other authors report no conflicts.

REFERENCES

1. Arribas F, Auricchio A, Boriani G, et al. Statistics on the use of cardiac electronic devices and electrophysiological procedures in 55 ESC countries: 2013 report from the European Heart Rhythm Association (EHRA). Europace 2014;16 Suppl 1:i1–i78.
2. Wood M, Goldberg S, Lau M, Goel A, Alexander D, Han F, Feinstein S. Direct measurement of the lethal isotherm for radiofrequency ablation of myocardial tissue. Circ Arrhythm Electrophysiol 2011;4:373–378.
3. Quesson B, de Zwart JA, Moonen CT. Magnetic resonance temperature imaging for guidance of thermotherapy. J Magn Reson Imaging 2000;12:525–533.
4. Jolesz FA, Hynynen K. Magnetic resonance image-guided focused ultrasound surgery. Cancer J Sudbury Mass 2001;8 Suppl 1:S100–S112.
5. Schlesinger D, Benedict S, Diederich C, Gedroyc W, Klibanov A, Larner J. MR-guided focused ultrasound surgery, present and future. Med Phys 2013;40.
6. Grissom WA, Rieke V, Holbrook AB, Medan Y, Lustig M, Santos J, McConnell MV, Pauly KB. Hybrid referenceless and multibaseline subtraction MR thermometry for monitoring thermal therapies in moving organs. Med. Phys. 2010;37:5014–5026.
7. Hey S, Cernicanu A, de Senneville BD, Roujol S, Ries M, Jaïs P, Moonen CTW, Quesson B. Towards optimized MR thermometry of the human heart at 3T. NMR Biomed 2012;25:35–43.
8. Nazarian S, Kolandaivelu A, Zviman MM, et al. Feasibility of real-time magnetic resonance imaging for catheter guidance in electrophysiology studies. Circulation 2008;118:223–229.
9. Campbell-Washburn AE, Rogers T, Xue H, Hansen MS, Lederman RJ, Faranesh AZ. Dual echo positive contrast bSSFP for real-time visualization of passive devices during magnetic resonance guided cardiovascular catheterization. J Cardiovasc Magn Reson 2014;16:88.
10. Hoffmann BA, Koops A, Rostock T, et al. Interactive real-time mapping and catheter ablation of the cavotricuspid isthmus guided by magnetic resonance imaging in a porcine model. Eur Heart J 2010;31:450–456.
11. Vergara GR, Vijayakumar S, Kholmovski EG, et al. Real-time magnetic resonance imaging–guided radiofrequency atrial ablation and visualization of lesion formation at 3 Tesla. Heart Rhythm 2011;8:295–303.
12. Ranjan R, Kholmovski EG, Blauer J, Vijayakumar S, Volland NA, Salama ME, Parker DL, MacLeod R, Marrouche NF. Identification and acute targeting of gaps in atrial ablation lesion sets using a real-time magnetic resonance imaging system. Circ Arrhythm Electrophysiol 2012;5:1130–1135.
13. Sommer P, Grothoff M, Eitel C, Gaspar T, Piorkowski C, Gutberlet M, Hindricks G. Feasibility of real-time magnetic resonance imaging-guided electrophysiology studies in humans. Europace 2013;15:101–108.
14. Grothoff M, Piorkowski C, Eitel C, et al. MR imaging-guided electrophysiological ablation studies in humans with passive catheter tracking: initial results. Radiology 2014;271:695–702.
15. Volland NA, Kholmovski EG, Parker DL, Hadley JR. Initial feasibility testing of limited field of view magnetic resonance thermometry using a local cardiac radiofrequency coil. Magn Reson Med 2013;70:994–1004.
16. Kolandaivelu A, Zviman MM, Castro V, Lardo AC, Berger RD, Halperin HR. Noninvasive assessment of tissue heating during cardiac radiofrequency ablation using MRI thermography. Circ Arrhythm Electrophysiol 2010;3:521–529..
17. de Senneville BD, Roujol S, Jaïs P, Moonen CTW, Herigault G, Quesson B. Feasibility of fast MR-thermometry during cardiac radiofrequency ablation. NMR Biomed 2012;25:556–562.
18. Hansen MS, Sørensen TS. Gadgetron: an open source framework for medical image reconstruction. Magn Reson Med 2013;69:1768–1776.
19. Griswold MA, Jakob PM, Heidemann RM, Nittka M, Jellus V, Wang J, Kiefer B, Haase A. Generalized autocalibrating partially parallel acquisitions (GRAPPA). Magn Reson Med 2002;47:1202–1210.
20. Black MJ, Anandan P. A framework for the robust estimation of optical flow. In Proceedings of the Fourth International Conference on Computer Vision, Berlin, 1993. p 231–236.
21. Roujol S, Ries M, Quesson B, Moonen C, Denis de Senneville B. Real-time MR-thermometry and dosimetry for interventional guidance on abdominal organs. Magn Reson Med 2010;63:1080–1087.
22. Pratikakis I, Barillot C, Hellier P, Memin E. Robust multiscale deformable registration of 3D ultrasound images. Int J Image Graph 2003;03:547–565.
23. Maclair G, Senneville BD de, Ries M, Quesson B, Desbarats P, Benois-Pineau J, Moonen CTW. PCA-based magnetic field modeling: application for on-line MR temperature monitoring. In: Ayache N, Ourselin S, Maeder A, eds. Medical Image Computing and Computer-Assisted Intervention—MICCAI. Lecture Notes in Computer Science. Heidelberg, Germany: Springer Berlin, 2007. p 411–419.
24. Vigen KK, Daniel BL, Pauly JM, Butts K. Triggered, navigated, multi-baseline method for proton resonance frequency temperature mapping with respiratory motion. Magn Reson Med 2003;50:1003–1010.
25. de Senneville BD, Ries M, Maclair G, Moonen C. MR-guided thermotherapy of abdominal organs using a robust PCA-based motion descriptor. IEEE Trans Med Imaging 2011;30:1987–1995.
26. Sapareto SA, Dewey WC. Thermal dose determination in cancer therapy. Int J Radiat Oncol Biol Phys 1984;10:787–800.
27. Weidensteiner C, Quesson B, Caire-Gana B, Kerioui N, Rullier A, Trillaud H, Moonen CTW. Real-time MR temperature mapping of rabbit liver in vivo during thermal ablation. Magn Reson Med 2003;50:322–330.
28. Köhler MO, Mougenot C, Quesson B, Enholm J, Le Bail B, Laurent C, Moonen CTW, Ehnholm GJ. Volumetric HIFU ablation under 3D guidance of rapid MRI thermometry. Med Phys 2009;36:3521.
29. Quesson B, Vimeux F, Salomir R, de Zwart JA, Moonen CTW. Automatic control of hyperthermic therapy based on real-time Fourier analysis of MR temperature maps. Magn Reson Med 2002;47:1065–1072.
30. Mougenot C, Quesson B, de Senneville BD, de Oliveira PL, Sprinkhuizen S, Palussière J, Grenier N, Moonen CTW. Three-dimensional spatial and temporal temperature control with MR thermometry-guided focused ultrasound (MRgHIFU). Magn Reson Med 2009;61:603–614.
31. Squara F, Latcu DG, Massaad Y, Mahjoub M, Bun S-S, Saoudi N. Contact force and force-time integral in atrial radiofrequency ablation predict transmurality of lesions. Europace 2014;16:660–667.